Journal of Cluster Science (2025) 36:16
https://doi.org/10.1007/s10876-024-02729-3

ORIGINAL PAPER

ZnO/PMMA Nanofibers for the Photocatalytic Water Remediation

Kinyas Polat[1] · **Elif Ant Bursalı**[2] · **Mürüvvet Yurdakoç**[2]

Received: 23 May 2024 / Accepted: 11 October 2024 / Published online: 3 December 2024

Abstract
In this study, a novel ZnO/PMMA nanofiber catalyst was fabricated using electrospinning, resulting in a barbed wire-like structure that enhances photocatalytic performance. The research aimed to investigate the material's effectiveness in degrading organic pollutants under UV light, providing a sustainable solution for water purification. Comprehensive characterization techniques, including XRD, XPS, SEM, EDS, and FTIR, were employed to analyze the crystal structure, micromorphology, and elemental composition of the catalyst. Photocatalytic degradation experiments showed that up to 91% degradation was achieved after 60 min of UV light irradiation at pH 11, with no significant bulk adsorption observed, confirming the dominance of the photocatalytic mechanism. The optimized pH of 11 was found to be ideal for achieving high degradation rates. This novel ZnO/PMMA nanofiber structure demonstrates significant potential for environmental applications, particularly in water purification, offering an efficient and sustainable approach to pollutant removal.

Keywords Nanofiber · Barbed wire · ZnO · PMMA · Electrospinning

Introduction

The large surface area of nanofiber structures greatly increases the contact with pollutants, which is why they are essential to photocatalysis. This characteristic is required to address the expanding issue of water pollution, which degrades water quality as a result of contaminants from domestic, commercial, and agricultural sources. Using photocatalysts like zinc oxide (ZnO) nanofibers becomes a vital tool for breaking down these contaminants into unharmful small molecules. It offers an efficient method for purifying water resources, thus reducing the environmental impact of pollution and contributing to the safeguarding of public health [1–13]. ZnO nanofibers stand out in photocatalysis due to their high surface area-to-volume ratio, enhancing light absorption and photocatalytic reactions. Their unique one-dimensional structure facilitates electron transport, reducing recombination rates and improving efficiency. There are so many methods to obtain nanofiber forms of ZnO that effectively decrease the band gap and hence increase the degrading yield of pollutants. In their 2021 study, Enculescu et al. developed a novel process for fabricating ZnO and TiO_2 nanotubes, showcasing enhanced photocatalytic efficiency. The method integrated electrospinning, magnetron sputtering, and calcination, yielding nanotubes with notably reduced band gaps compared to their bulk counterparts. Through the photocatalytic degradation of Rhodamine B, they demonstrated remarkable efficiencies of approximately 55% for ZnO and 95% for TiO_2 nanotubes, utilizing only 0.5 mg of nanotubes in 10 mL dye solutions, underlining the potential of these nanostructures in environmental applications. [14]. Jia et al. investigated the pH-responsive behavior and photocatalytic characteristics of ZnO nanofibers modified by grafting poly (methyl methacrylate) (PMMA) in their 2020 study. They improved the adaptability and efficiency of ZnO nanofibers in photocatalysis, especially at different pH levels, by using this novel approach. According to their research, modified ZnO nanofibers can greatly enhance photocatalytic processes, which might lead to improvements in environmental remediation and water treatment technologies [15]. To further explore ZnO applications in photocatalysis, Di Mauro et al. (2017) moved from thin films to different nanostructures. Their study highlighted the higher

✉ Kinyas Polat
kpolat@sinop.edu.tr

[1] Department of Metallurgical and Materials Science Engineering, Faculty of Engineering and Architecture, Sinop University, Sinop 57000, Türkiye

[2] Department of Chemistry, Faculty of Science, Dokuz Eylül University, Izmir 35390, Türkiye

photocatalytic activity of ZnO materials with nanostructures as opposed to thin-film equivalents. In particular, ZnO nanorods performed better in photocatalysis when placed on a 3 nm thin layer [16]. In their 2021 study, Mohammed explored the enhancement of structural, optical, electrical properties, and photocatalytic applications of ZnO/PMMA nanocomposite membranes. Their research aimed at developing multifunctional membranes, emphasizing the integration of ZnO nanoparticles with PMMA to improve not only the material's physical properties but also its effectiveness in photocatalytic degradation [17]. Di Mauro et al. (2020) investigated the photocatalytic potential of a ZnO/PMMA nanocomposite by synthesizing it by low-temperature atomic layer deposition. By breaking down sodium lauryl sulfate and methylene blue (MB) dye in water, they evaluated the nanocomposites' photocatalytic activity and showed how well the materials removed pollutants [18]. Gupta et al. created trimetallic composite nanofibers in their 2020 study with the twin goals of photocatalytic dye breakdown in mixed dye water and antibacterial activity. These Ag/ZnO/TiO_2-based nanofibers shown notable success in the degradation of many dyes, such as fuchsin (MB 93.4%), Rhodamine (Rh 34.6%), auramine-O (Au 65.0%), and MB 93.4%, suggesting possible applications in environmental remediation and water purification [19]. Varkey and Jose (2022) examined the optical and structural characteristics of ZnO–poly(styrene–co-methyl methacrylate) nanofiber composites that were electrospun. The goal of their work was to combine ZnO nanofibers with a polymer matrix to improve their functioning in photocatalytic processes [20]. Preda, Evanghelidis et al. (2015) presented the electroless deposition of ZnO crystallites on electrospun PMMA fiber mats, whereby the deposition, activation, and sensitization steps are combined into one process. They were able to effectively coat the fibers with ZnO by submerging the PMMA mats in certain solutions for each step. This technique offers a way to add ZnO's semiconductor qualities to PMMA mats, which may improve their photocatalytic capabilities [21]. Matei et al. (2018) investigated the electrodeposition of ZnO nanostructures to achieve hierarchical functionalization of electrospun fibers. Through the controlled and homogeneous deposition of ZnO, their technique aims to improve the surface characteristics of the fibers for a variety of applications, including photocatalysis [22]. ZnO/NiO Janus-like nanofibers with remarkable photocatalytic effectiveness were created by Liu et al. (2018). In just one hour, the nanofibers were able to degrade malachite green by up to 96% under 365 nm UV light [23]. Through electrospinning, Pascariu et al. (2021) created special lanthanide-doped ZnO nanoparticles (Sm, La, Er) reinforced in PVDF membranes. These innovative materials attained up to 96.33% efficiency, demonstrating previously unheard-of rates of MB and Rh degradation under visible light. PVDF/ZnO: La (37%) membranes maintained 98% efficiency and showed remarkable photocatalytic stability [24]. In order to break down MB in the presence of UV radiation and sunshine, Abu-Dalo, Al-Rosan, and Albiss (2021) created cellulose acetate membranes containing embedded ZnO nanostructures. Compared to UV (30%), sunlight irradiation shows a greater deterioration rate of 75% [25]. Morselli et al. (2017) used a two-step procedure comprising electrospinning and heat treatment to create PMMA fibrous membranes embedded with in situ produced ZnO nanoparticles. Regardless of the amount of precursor used, the process produces crystalline ZnO nanoparticles with branching nanoparticles (50–140 nm) on the fibers' surface and spherical ones (~7 nm) within. These multipurpose materials show promise for use in photocatalysis, wound care, filtration, and UV shielding because to their UV-responsive wettability, improved thermal stability, and antibacterial qualities [26].

The integration of ZnO nanoparticles into PMMA via the electrospinning technique offers a novel approach to fabricating nanocomposites with high surface area and enhanced photocatalytic performance. This method not only prevents the aggregation of ZnO nanoparticles but also facilitates the separation and recovery of the photocatalyst after degradation processes. The literature summary is given in Table 1.

There has been a limited number of studies to deeply understand and discover the potential of ZnO/PMMA nanofibers in photocatalysis applications therefore, The original aspect of this work is the revolutionary incorporation of ZnO into PMMA nanofibers by electrospinning, which retains the fibers' mechanical integrity while improving their photocatalytic activities. This method produces a distinct barbed wire design with a high surface area-to-volume ratio, which dramatically increases pollutant degradation. While earlier research has investigated ZnO nanofibers in photocatalysis, the approach reported here avoids the usual problem of aggregation encountered in ZnO nanoparticles, also this research achieves a barbed wire-like architecture of ZnO within the fibers, which enhances surface area resulting in improved photocatalytic efficiency.

Furthermore, this study emphasizes the multifunctionality of ZnO/PMMA nanofibers, which have prospective uses not only in environmental remediation but also in antibacterial therapies and ultraviolet protection. The ability to produce these nanofibers without sacrificing their structural integrity while preserving strong photocatalytic efficacy is a major improvement. This work adds to the current body of knowledge by investigating a unique manufacturing approach that improves the material's functioning across a wide range of applications, providing a scalable and effective solution for water purification and environmental sustainability. The enhanced electron transport and lower recombination rates

Table 1 Literature summary

Study	Objective	Materials	Methods	Key Findings
Enculescu et al. [14]	Fabricate ZnO and TiO2 nanotubes for enhanced photocatalysis	ZnO, TiO2 nanotubes	Electrospinning, magnetron sputtering, calcination	ZnO showed 55% efficiency; TiO2 showed 95% efficiency in Rh degradation.
Jia et al. [15]	Investigate pH-responsive behavior and photocatalytic characteristics	ZnO nanofibers, PMMA	Grafting ZnO nanofibers with PMMA	Improved adaptability and efficiency of ZnO nanofibers in photocatalysis at different pH levels.
Di Mauro et al. [16]	Compare photocatalytic activity of ZnO nanostructures vs. thin films	ZnO nanostructures	Thin film deposition, nanostructure fabrication	ZnO nanorods showed better photocatalytic performance than thin films.
Mohammed et al. [17]	Enhance properties and applications of ZnO/PMMA nanocomposites	ZnO nanoparticles, PMMA membranes	Fabrication of multifunctional membranes	Enhanced structural, optical, and photocatalytic properties.
Di Mauro et al. [18]	Investigate ZnO/PMMA nanocomposite for pollutant degradation	ZnO/PMMA nanocomposites	Low-temperature atomic layer deposition	Successful degradation of sodium lauryl sulfate and MB dye.
Gupta et al. [19]	Create trimetallic nanofibers for photocatalysis and antibacterial action	Ag/ZnO/TiO2 nanofibers	Fabrication of nanofibers	Effective degradation of various dyes (93.4% MB, 34.6% Rh, etc.) and antibacterial properties.
Varkey and Jose [20]	Improve photocatalysis through ZnO-polymer composites	ZnO–poly(styrene–co-methyl methacrylate) nanofibers	Electrospinning	Improved optical and structural characteristics for enhanced photocatalytic function.
Preda et al. [21]	Investigate ZnO coating on PMMA fiber mats	ZnO crystallites, PMMA	Electroless deposition of ZnO on PMMA	ZnO coating improved photocatalytic capabilities of PMMA mats.
Matei et al. [22]	Achieve hierarchical functionalization of fibers	ZnO nanostructures, electrospun fibers	Controlled electrodeposition of ZnO on fibers	Enhanced surface characteristics and functionality of electrospun fibers.
Liu et al. [23]	Fabricate Janus-like ZnO/NiO nanofibers	ZnO/NiO nanofibers	Electrospinning	Achieved 96% degradation of malachite green under UV light.
Pascariu et al. [24]	Create lanthanide-doped ZnO nanoparticles for photocatalysis	ZnO doped with Sm, La, Er, PVDF membranes	Electrospinning	Achieved up to 96.33% dye degradation, with ZnO: La membranes maintaining 98% efficiency.
Abu-Dalo et al. [25]	Create ZnO nanostructure-embedded cellulose acetate membranes	ZnO nanostructures, cellulose acetate membranes	Fabrication of cellulose acetate membranes with embedded ZnO	Achieved 75% pollutant degradation under sunlight irradiation.
Morselli et al. [26]	Fabricate PMMA/ZnO membranes for photocatalysis	ZnO nanoparticles, PMMA fibrous membranes	Electrospinning and heat treatment	Created ZnO nanoparticles with improved photocatalytic and antibacterial properties.

inside ZnO nanofibers illustrate their better performance over traditional nanocomposites.

Experimental

Materials and Methods

ZnO was supplied by Molumer LLC. PMMA (Product code 445746, Mw 350,000 g/mol measured by GPC) was purchased from Sigma Aldrich. Brilliant Blue (BB) dye was obtained from Sigma-Aldrich (Product Code 1.12553). The molecular structure of the dye is given in Fig. 1. N, N-dimethylformamide (DMF) was purchased from Sigma-Aldrich (Product Code 227056).

Preparation of ZnO/PMMA Nanofibers

The polymer fiber mats were obtained by electrospinning using a solution of 10 wt% PMMA in N, N-dimethylformamide (DMF) consisting of ZnO powder 0.2 g/mL of PMMA solution. The solution was introduced into the 10 mL syringe pump controlled with a microcontroller and a step motor. A rotatory copper foil-coated, 10 cm wide cylindrical 3d printed collector was used for both stretching and collecting the nanofibers extruded from a metallic hollow needle connected to a high voltage power supply (30 kV Chengdu Chuangyu Xinjie Technology LLC). The electrospinning process parameters were: 1 ml/h solution flow rate, 30 kV driving high voltage applied, and 3 cm needle-to-metal collector distance. The obtained electrospun fiber mats were removed from the collector electrode to use in the photocatalysis.

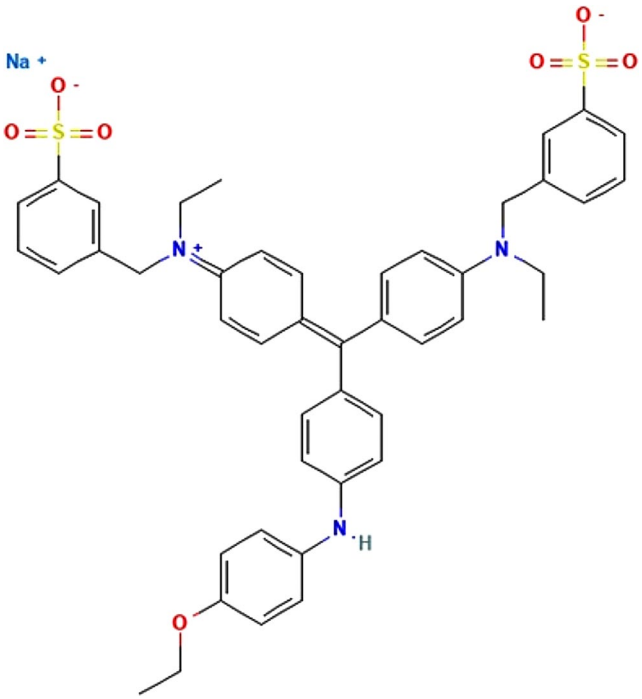

Fig. 1 Structure of the BB dye

Characterization

The phase of ZnO/PMMA nanofibers was accurately determined utilizing an X-ray powder diffractometer (Thermo Scientific ARL X'TRA) using Cu(Kα) radiation (λ = 1.5415 × 10–10) operating at 40 kV and 30 mA. A detailed crystalline structure analysis, phase composition, and particle dimension analysis were carried out. To assess the light absorption properties hence photocatalytic performance, an ultraviolet–visible spectrophotometer (UV–Vis, Shimadzu UV 1800) was employed. For determining a comprehensive examination of the surface morphology and microstructural features of the catalyst, including high-resolution visuals of the surface, revealing the nanofibers' texture, distribution, and overall topography, a scanning electron microscope (ZEISS EVO HD15) was utilized. Elemental composition and distribution within the materials were analyzed using an energy dispersive spectrum (EDS) detector coupled with the SEM. Additionally, the oxidation state of the ZnO powder, an essential parameter influencing the chemical and photocatalytic properties of the nanofibers, was determined through X-ray photoelectron spectroscopy (XPS) analysis (Thermo Scientific K-Alpha). Finally, FTIR spectroscopy (Perkin Elmer BX II model) was used to interpret the molecular bonds belonging to both ZnO and PMMA.

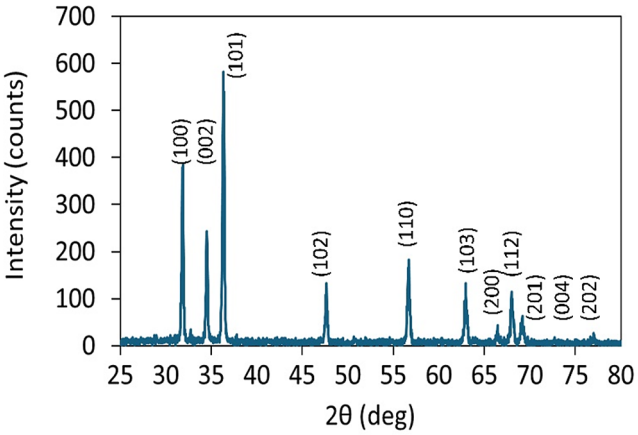

Fig. 2 XRD patterns of the ZnO/PMMA

Photocatalytic Activity

The samples' photocatalytic activity was evaluated in a closed box with a UV light (Osram 300 W) positioned vertically next to a beaker filled with 100 mL of BB solution. A magnetic stirrer was used to ensure constant agitation at ambient temperature. A UV-vis spectrophotometer was used to assess the absorption of a small sample of the irradiated solution that was collected at different intervals. Degradation rates were assessed using Eq. 1:

$$\eta \ (\%) = \left[\frac{C - C_0}{C_0}\right] x100 \tag{1}$$

The degradation rate is denoted by η in the equation, the stock solution absorbance is represented by C_0, and the absorbance at a certain instant is denoted by C. Significant factors including pH, catalyst quantity, and dye concentration were also assessed to determine the ideal circumstances for photocatalysis. Additionally, dark, and blank trials were conducted to ensure that no contribution came from photolysis or adsorption.

Results and Discussion

XRD Characterization

In Fig. 2, the ZnO powder's X-ray diffraction pattern is shown. Diverse peaks, including (100), (002), (101), (102), (110), (103), (200), (112), and (201), confirm the hexagonal wurtzite structure of ZnO powder (JCPDS Card No: 36-1451). This indicates that the wurtzite phase is very pure since no further peaks associated with impurities are seen [27–28]. The average crystallite size of the ZnO particles was calculated using Debye-Scherrer equation [29] (Eq. 2) and determined as 30.32 nm.

$$D_p = \frac{0{,}94\lambda}{\beta_{1/2} cos\theta} \quad (2)$$

Where D_p represents the average crystallite size, β is the line broadening in radians (also referred as Full-Width at Half Maximum (FWHM), θ stands for the Bragg angle and λ is the X-ray wavelength. 0.94 is a numerical factor frequently referred to as the crystallite-shape factor. The peaks selected for calculation, FWHM values and determined crystallite sizes were all given in Table 2.

Table 2 Crystallite size determination of the ZnO/PMMA

Peak position (2 Theta)	d_{hkl}	FWHM	Crystallite size D (nm)
31.85	(100)	0.24	34.34
34.52	(002)	0.24	34.78
36.34	(101)	0.25	32.82
47.63	(102)	0.28	30.91
56.68	(110)	0.32	28.52
62.95	(103)	0.33	28.08
68.03	(112)	0.35	27.50
69.16	(201)	0.38	25.67
Average Crystallite Size (D_{AVR})			**30.32 nm**

FTIR Characterization

Figure 3 displays the ZnO/PMMA photocatalyst's FTIR spectrum. FTIR spectra were recorded in the 4000–400 cm^{-1} range with a resolution of 4 cm^{-1}, and 50 scans were averaged for each sample. Due to hydrogen-bonded OH stretching vibration brought on by a small amount of moisture after exposure to the atmosphere, a faint band is seen at 3440 cm^{-1}. The peaks observed at 2957 cm^{-1} and 2885 cm^{-1} were attributed to the symmetric and asymmetric stretching vibrations of the methylene groups, respectively. A CO stretching vibration of the PMMA is responsible for the absorption band at 1736 cm^{-1} [30]. The vibrations caused by bending deformation, CH_3 symmetric deformation, wagging deformation, twisting deformation, and wagging deformation are responsible for the absorption bands at 1475, 1386, 1238, and 908 cm^{-1}, respectively. The OCH_3 deformation vibrations and the COC symmetric stretching vibrations, which are PMMA's fingerprint vibrations, are detected at 908 and 1386 cm^{-1}, respectively. The bending, ring out of plane, or rocking deformation vibrations of PMMA are responsible for the absorption bands seen in 840 cm^{-1} areas [30]. The hexagonal ZnO structure is responsible for the peaks at 510 and 431 cm^{-1} [31].

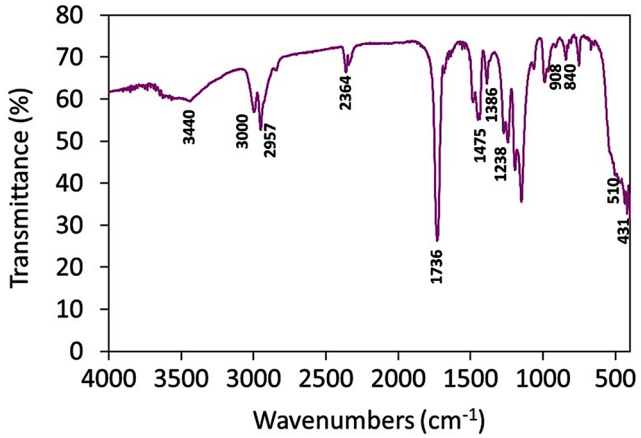

Fig. 3 FTIR spectrum of ZnO/PMMA

XPS Characterization

Figure 4 reports the XPS spectrum of the electrospun ZnO/PMMA fibers, which provide important information on chemical bonding of the fibers. At 285.5, 286.4, and 288.2 electron volts (eV), three different signals are seen in the C1s spectrum, which is concerned with the electron binding energies connected to carbon atoms in different chemical environments.

The CO bond, which is a part of the PMMA structure, is represented by the peak at 285.5 eV. This signal is suggestive of the PMMA polymer backbone, in which a carbon atom is singly linked to an oxygen atom (in the ester group) in each methyl methacrylate unit. The stability and physical characteristics of the polymer depend heavily on this connection. The carbon atoms in the carboxylate groups

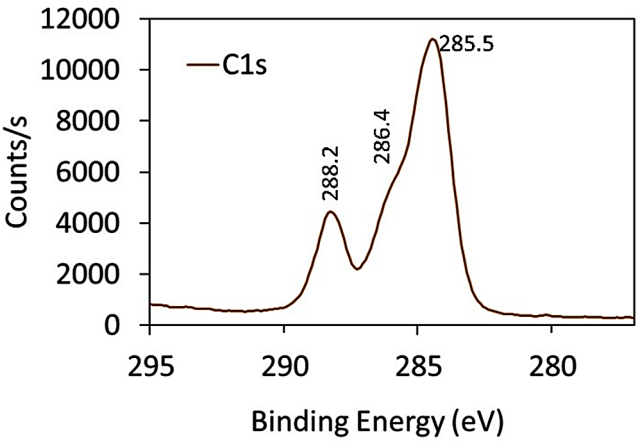

Fig. 4 XPS spectrum of ZnO/PMMA in the C1s binding energy zone

(COO), which are a component of the PMMA structure, are responsible for the signal at 286.4 eV. The peak indicates the presence of ester functionalities, a fundamental group in PMMA's backbone, which may influence the stability and dispersion of nanoparticles within the polymer matrix through interactions with ZnO nanoparticles. The PMMA polymer's aliphatic carbon, is represented by the peak seen at 288.2 eV [32].

The oxygen-containing functional groups on the fiber surface are explained by two peaks in Fig. 5 that are located

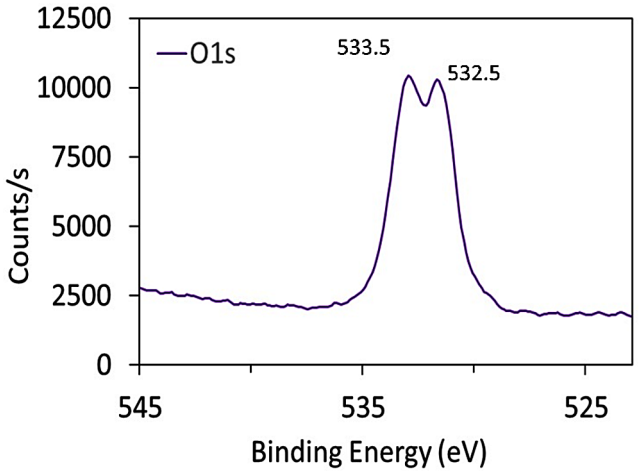

Fig. 5 XPS spectrum of ZnO/PMMA in the O1s binding energy zone

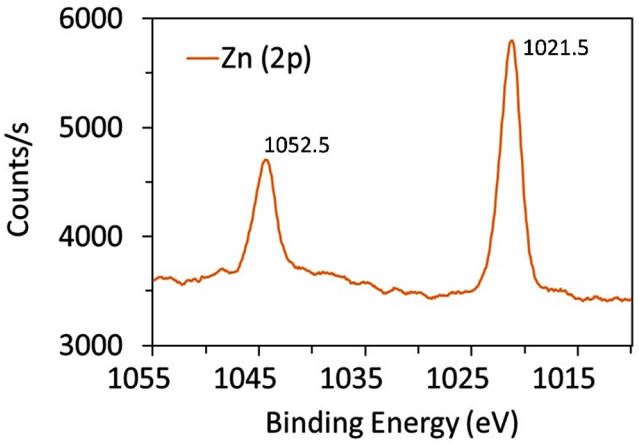

Fig. 6 XPS spectrum of ZnO/PMMA in 2p binding energy zone

at 532.5 and 533.5 electron volts (eV). This illustrates the complex chemical environment that is made possible by the PMMA matrix and the electrospinning process. The peak at 532.5 eV is caused by the oxygen atom-containing carbonyl (C = O) groups. The second signal, which was seen at 533.5 eV, is indicative of oxygen atoms found in PMMA's methoxy carbonyl (CH_3-O-C=) groups [32].

The spin-orbit components, 2p3/2 and 2p1/2 of ZnO component of the nanofibers are described in Fig. 6.

The Zn 2p3/2 spin-orbit component is represented by the peak at 1021.5 eV. This binding energy is exclusive to zinc in ZnO and indicates that zinc is present in its oxidized state (Zn^{2+}). The exact location of this peak suggests a distinct ZnO crystalline structure inside the composite and may provide information about the chemical environment of zinc atoms. A sign of the ZnO nanoparticles' effective incorporation into the PMMA matrix is the Zn 2p3/2 peak. Zinc's oxidation state inside the composite is further confirmed by the second peak, which is positioned at 1052.5 eV and is attributable to the Zn 2p1/2 spin-orbit component. The spin-orbit splitting, which separates the Zn 2p3/2 and Zn 2p1/2 peaks, is in agreement with published values for ZnO, supporting the presence of ZnO in the PMMA matrix. The ZnO phase's purity and chemical integrity in the composite material are confirmed by the appearance of this peak in conjunction with the Zn 2p3/2 component [32–33].

SEM Characterization

A detailed view of nanofibers embedded with ZnO nanoparticles is seen in Fig. 7, where the nanoparticles have a structure resembling barbed wire. The nanofibers themselves have a high surface area to volume ratio due to their tiny production with the electrospinning technique, as seen by their diameters of less than 500 nm. ZnO nanoparticles which are distinguished by their diameters of less than 100 nm are embedded in these fibers. This size distribution suggests that the synthesis process was well-regulated to produce nanoparticles that were uniformly dispersed throughout the fiber matrix.

The elemental composition of the nanofibers was determined by performing EDS analysis on different sections of the samples. The objective of the investigation was to measure the distribution of zinc (Zn), oxygen (O), and carbon (C) in the fibers in order to shed light on the addition of ZnO nanoparticles to the PMMA matrix. Zinc (Zn), oxygen (O), and carbon (C) levels were found using EDS analysis, however, it is not a precise quantitative method. The percentages are 77%, 15%, and 7.6%, respectively. These findings show a strong carbon presence, which is in line with the carbon-rich backbone of the PMMA polymer. The ZnO nanoparticles and the polymer matrix are both responsible for the oxygen content, whereas the ZnO particles embedded in the nanofibers are the direct cause of the zinc content. The measured zinc and oxygen percentages show that the ZnO nanoparticles were successfully embedded, while the high carbon content confirms the structural integrity of the PMMA matrix. EDS study validates the potential of ZnO/PMMA nanofibers for photocatalytic processes.

Photocatalytic Activity

In the absence of light, pollutants or model dyes are adsorbed onto the photocatalyst surface in a process known as "dark adsorption," while photolysis is the breakdown of chemical compounds by the radiation source's photons. To ensure that the observed activity is solely attributable to the photocatalytic reactions facilitated by the ZnO/PMMA nanofibers, the influence of dark adsorption and photolysis were isolated at the beginning by waiting at least 6 h in the dark with catalyst material and under UV light without catalyst material. It was observed that neither adsorption by

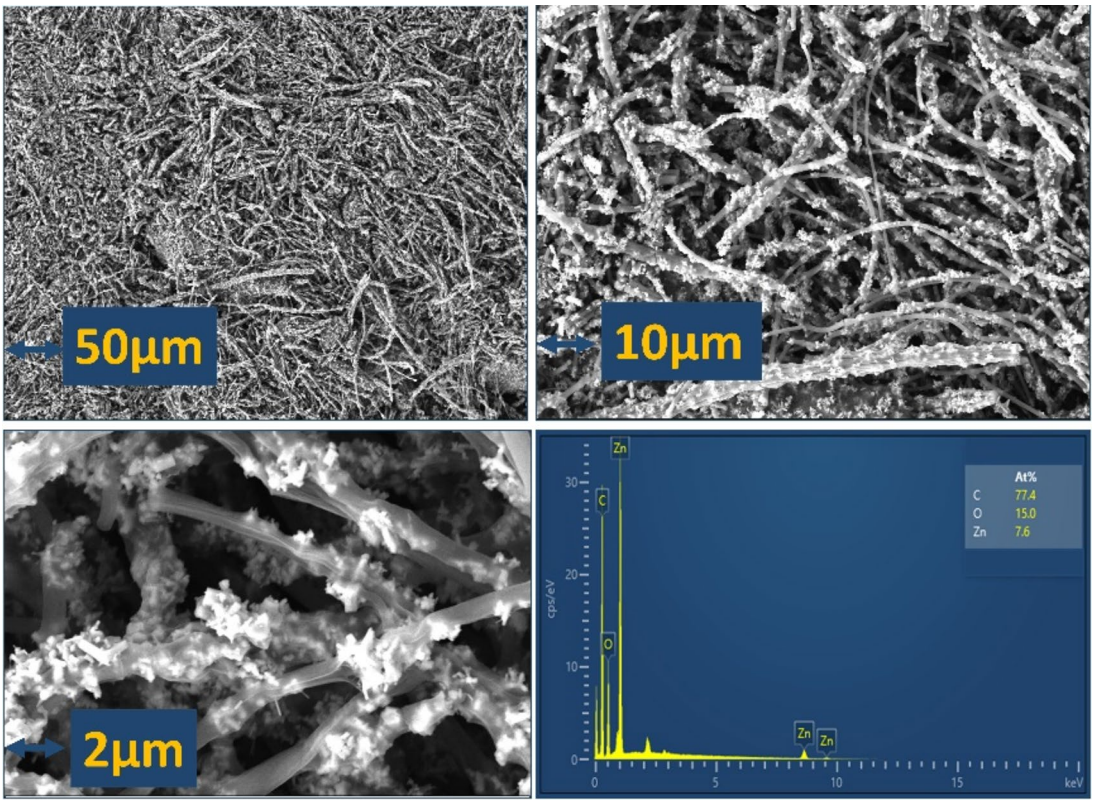

Fig. 7 SEM and EDS spectrum images of ZnO/PMMA

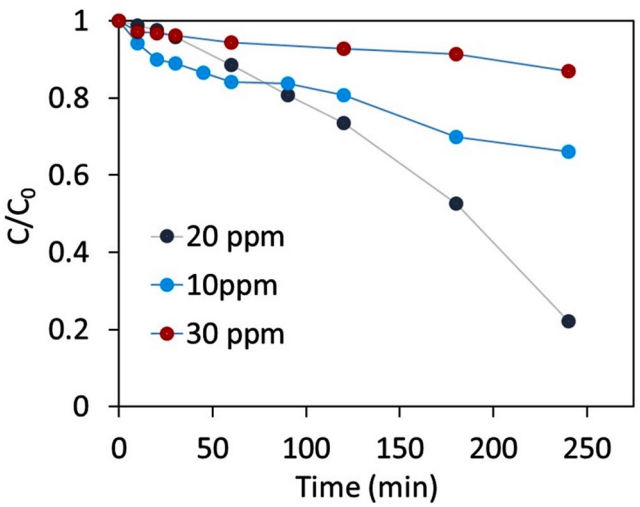

Fig. 8 Effect of dye concentration

the catalyst material nor a photolysis reaction was encountered. This result was expected due to the lack of attraction of hydrophobic PMMA chains towards hydrophilic BB dye molecules.

The dye concentration, or the quantity of dye in a given volume of solution, plays a critical role in the assessment of photocatalytic activity and may have a major impact on the speed of the photocatalytic process. Up to a certain point, a greater dye concentration may result in a faster rate of reaction; but, since the dye molecules absorb too much light, the reaction may then become saturated or even halted. The effect of dye concentration was evaluated using three different concentrations and the results were plotted as degradation rate comparison in Fig. 8.

Figure 8 suggests that a dye concentration of 20 ppm is optimal for photocatalytic activity. This observation can be attributed to two primary reasons. Firstly, at a higher concentration of 30 ppm, the dye solution becomes sufficiently dark to prevent the penetration of light to the catalyst's active sites, thereby hindering the photocatalytic process. Secondly, at 10 ppm, the solution faces challenges with concentration-dependent reaction kinetics, which impede the dye molecules from efficiently reaching the active regions of the catalyst, resulting in a reduced rate of degradation. Consequently, a dye concentration of 20 ppm sets a balance, offering a reasonable degradation rate by avoiding these issues.

Another important element is the dye solution's pH, which influences the photocatalyst's surface characteristics, which in turn impacts the catalyst's capacity to adsorb dye molecules and take part in the photocatalytic process. The stability of the dye and the photocatalyst, as well as the rate at which the reactions occur, may all be impacted by pH. The influence of pH on degradation was evaluated using pH

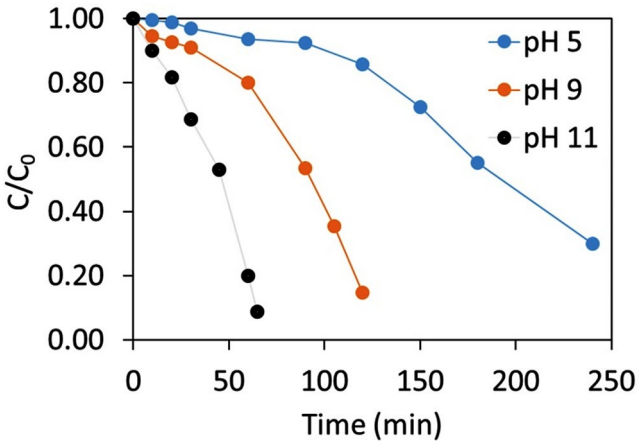

Fig. 9 Effect of solution pH

values selected from three regions namely mildly acidic (pH 5), moderate basic (pH 9), and highly basic (pH 11). Results were introduced in Fig. 9. A rate increase towards a highly basic region was observed.

This situation can be clearly expressed when taking into account the photocatalysis mechanisms that occur on the catalyst surface. The photocatalytic degradation mechanism [34] on ZnO/PMMA nanofibers is driven by the generation of electron-hole pairs when exposed to UV light, as depicted in Fig. 10. In a basic solution, the concentration of hydroxyl ions (OH^-) increases, facilitating key reactions that drive the degradation process. Upon UV light irradiation, ZnO absorbs photons with energy greater than its bandgap, exciting electrons (e^-) from the valence band to the conduction band, leaving behind holes (h^+) in the valence band. The photogenerated holes (h^+) in the valence band react with the abundant hydroxyl ions (OH^-) in the solution, producing highly reactive hydroxyl radicals (OH•), which are potent oxidizing agents. These hydroxyl radicals attack and break down the organic pollutants, initiating a series of oxidation reactions. The more hydroxyl ions present in the basic medium, the more hydroxyl radicals are produced, which accelerates the photocatalytic degradation rate. Simultaneously, the excited electrons in the conduction band are captured by dissolved oxygen molecules (O_2) in the solution, reducing them to superoxide radicals (O_2•$^-$). These superoxide radicals undergo further reactions, forming additional hydroxyl radicals through chain reactions. The hydroxyl radicals (OH•) and superoxide radicals (O_2•$^-$) generated in these reactions are highly reactive and play a critical role in degrading the organic dye molecules into smaller, harmless products such as CO_2 and H_2O. The chain reactions occurring in photocatalytic process can be defined as below reactions;

$$ZnO + h\nu \rightarrow e^-_{CB} + h^+_{VB}$$

$$h^+_{VB} + OH^- \rightarrow OH\bullet$$

$$O_2 + e^-_{CB} \rightarrow O_2\bullet^-$$

$$O_2\bullet^- + H_2O \rightarrow OH\bullet + OH^- + O_2$$

$$\text{Dye (Pollutant)} + OH\bullet\ /O_2\bullet^- \rightarrow \text{Degradation Products } (CO_2,\ H2O,\ \text{etc.})$$

Lastly, the amount of catalyst used is directly related to the available active sites for the photocatalytic reaction. A sufficient amount of catalyst is necessary to ensure that there are enough active sites to interact with the dye molecules. In Fig. 11 the effect of catalyst amount on the photocatalytic

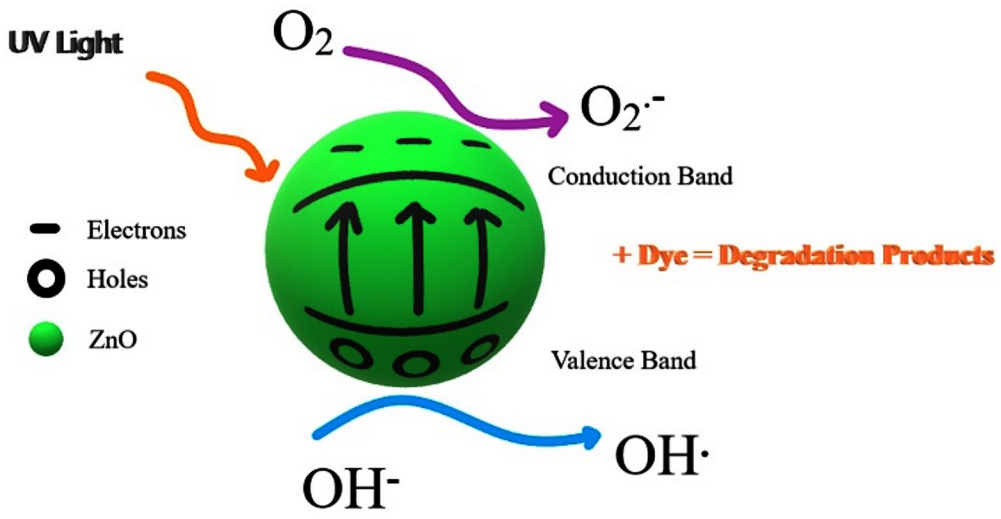

Fig. 10 Mechanism of photocatalytic degradation on ZnO/PMMA surface

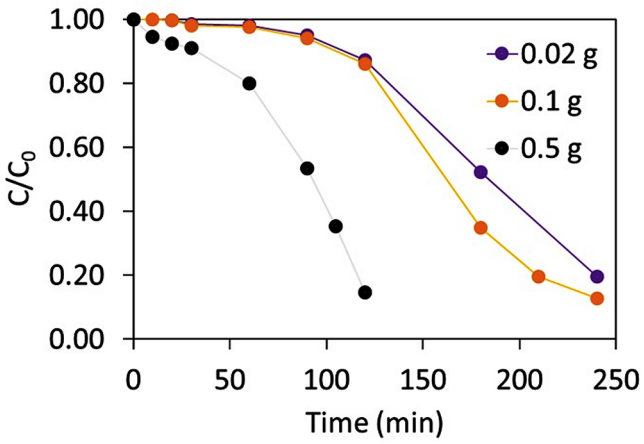

Fig. 11 Effect of catalyst amount

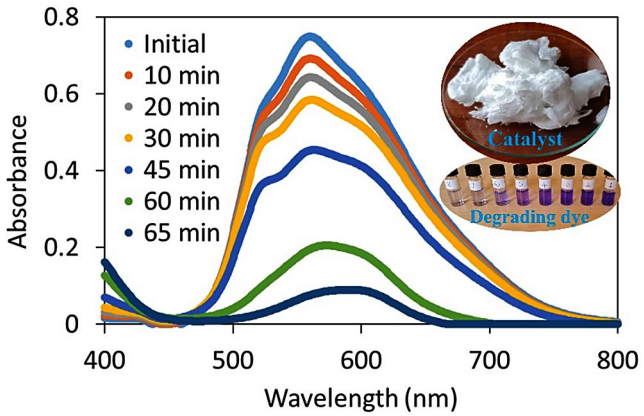

Fig. 12 Degrading dye under UV light

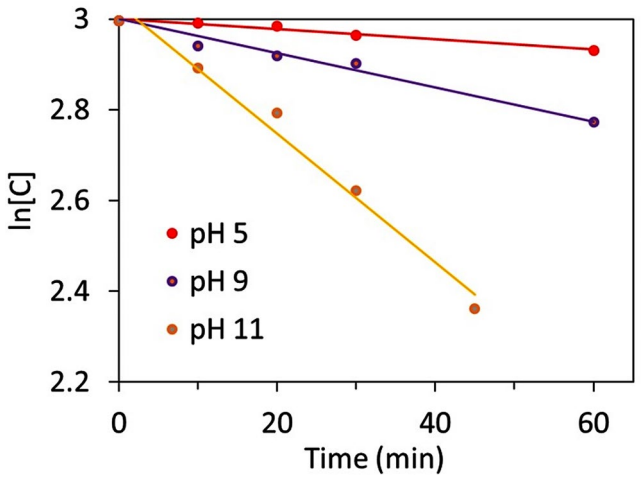

Fig. 13 First-order kinetic model fitting

activity was plotted. It was observed that as the catalyst amount increases the rate of reaction was found to increase accordingly. A highly reasonable rate was obtained when 0.5 g of catalyst material was used. This is because there are more vacant catalyst sites accessible at greater catalyst concentrations.

According to this study, 0.5 g of catalyst, a pH 11 dye solution, and a dye concentration of 20 ppm have been found to be the ideal parameters for the ZnO/PMMA nanofiber catalyst structure. A good picture of how the photocatalyst was effective for degrading the dye under UV illumination is visualized in Fig. 12.

Table 3 Summary of the kinetic study

pH	Rate constant (k) (s^{-1})	R^2 value
5	0.0011	0.97
9	0.0038	0.98
11	0.0142	0.98

Kinetics of Photocatalysis

Reaction kinetics must be understood to be scaled up from laboratory to industrial photocatalytic processes. It guarantees that the optimum reaction conditions in the laboratory may be successfully transferred to bigger systems, resulting in predictable variations in reaction speeds and efficiency. Figure 13 presented the kinetic assessment in which the degradation of dye with ZnO/PMMA catalyst obeys the first-order kinetics. According to first-order kinetics, the pace of the reaction is dependent solely on the concentration of one reactant, the pollutant or dye that is being broken down. Equation 3 defines first-order kinetics.

$$\ln [C] = \ln [C_0] - kt \tag{3}$$

Where C, C_0, k, and t stand for the dye concentration at any given time, the dye's starting concentration, the reaction rate constant, and time. First-order kinetics is shown by a linear graph of t vs. ln C.

For pH 5, pH 9, and pH 11, the corresponding reaction rate constants (k) and R^2 values which indicate the degree of linearity and speed were found to be 0.0011 s^{-1}, 0.0038 s^{-1}, 0.0142 s^{-1}, and 0.97, 0.98, and 0.98, respectively. Summary of the kinetic parameters found was given in Table 3. pH 11 is the point at which the fastest reaction happens, according to the data likely due to increased hydroxyl ion availability and subsequent radical formation. To provide a more comprehensive understanding, the zero charge point of the ZnO/PMMA catalyst should be considered. The zero charge point defines the pH at which the catalyst surface is neutral, influencing its ability to adsorb or repel dye molecules.

Table 4 Best performing parameters

Parameter	Value	Rate constant (k) (s^{-1})	R^2 value
Dye Concentration	20 ppm	0.0142	0.98
pH	11	0.0142	0.98
Catalyst Amount	0.5 g	0.0142	0.98

For ZnO, the zero charge point typically occurs around pH 9. Above this pH, the catalyst surface becomes negatively charged, promoting interaction with positively charged dye molecules, thus enhancing photocatalytic activity at pH 11. It is possible to draw the conclusion that the availability of dye molecules on the active surfaces of the photocatalyst surface at any given time influences the rate increase or decrease in first-order kinetics. The poor reaction rate at 10 ppm dye concentration may also be explained by this circumstance. The best performing degradation parameters were summarized in Table 4 for clarity.

Conclusion

This work reports the effective synthesis of a new ZnO/PMMA nanofiber catalyst with a distinctive barbed wire-like shape by the use of the electrospinning process. Under UV light irradiation at pH 11, the catalyst demonstrated exceptional photocatalytic degradation activities, degrading the dye up to 91% in 60 min.

The XRD analysis confirmed ZnO's hexagonal wurtzite structure, which has an average crystallite size of around 30.32 nm. Zinc's oxidation state as Zn^{2+} and the inclusion of ZnO particles into the PMMA matrix were confirmed by the XPS findings. Less than 500 nm in nanofiber diameter was shown by SEM imaging. With the matching reaction rate constants (k) and R^2 values of 0.0011 s^{-1}, 0.0038 s^{-1}, 0.0142 s^{-1}, and 0.97, 0.98, and 0.98, the first-order rate rule was in accordance with the reaction. The results of this study enable further investigation into the use of photocatalytic materials's design.

Author Contributions KP designed the study, prepared the catalyst materials with the electrospinning method, and wrote the manuscript. MY, and EAB carried out the photocatalytic degradation experiments. All authors reviewed the manuscript.

Funding No funding is applicable.

Data Availability No datasets were generated or analysed during the current study.

Declarations

Ethical Approval There are no ethical issues in this article.

Competing Interests The authors declare no competing interests.

References

1. G. Panthi, M. Park, H. Y. Kim, S. Y. Lee, and S. J. Park (2015). J. Ind. Eng. Chem. 21, 26.
2. M. M. Sabzehmeidani, M. Ghaedi, and H. Karimi (2021). Interface Sci. Tech. 32, 625.
3. A. Cordoba, C. Saldias, M. Urzúa, M. Montalti, M. Guernelli, M. L. Focarete, and A. Leiva (2022). Nanomaterials. 12, 756.
4. D. Ponnamma, J. J. Cabibihan, M. Rajan, S. S. Pethaiah, K. Deshmukh, J. P. Gogoi, S. S. K. Pasha, M. B. Ahamed, J. Krishnegowda, B. N. Chandrashekar, A. R. Polu, and C. Cheng (2019). Mater. Sci. Eng. C. 98, 1210.
5. W. Liu and H. Zhang (2024). *Electrospinning: Fund. Methods App*. 283.
6. H. Chen, M. Huang, Y. Liu, L. Meng, and M. Ma (2020). Sci. Total Environ. 739, 139944.
7. V. Melinte, L. Stroea, and A. L. Chibac-Scutaru (2019). *Catalysts*. 9, 986.
8. A. M. Nasir, N. Awang, J. Jaafar, A. F. Ismail, M. H. D. Othman, M. A. Rahman, F. Aziz, and M. A. M. Yajid (2021). J. Water Process. Eng. 40, 101878.
9. S. Asgari, G. M. Ziarani, A. Badiei, F. Ajalloueian, and Y. Vasseghian (2022). Environ. Res. 215, 114296.
10. A. D. Sekar and M. Manickam (2019). Water Wastewater Treat. Techn. 469.
11. F. H. Abdullah, N. A. Bakar, and M. A. Bakar (2022). J. Hazard. Mater. 424, 127416.
12. P. G. Ramos, L. A. Sánchez, and J. M. Rodriguez (2022). J. Sol-Gel Sci. Tech. 102, 105.
13. S. Agarwal, A. Greiner, and J. H. Wendorff (2013). Prog. Polym. Sci. 38, 963.
14. M. Enculescu, A. Costas, A. Evanghelidis, and I. Enculescu (2021). *Nanomaterials*. 11, 1305.
15. S. Jia, Q. Wang, J. Peng, J. Gao, and D. Tang (2020). SN Appl. Sci. 2, 1.
16. A. Di Mauro, M. E. Fragalà, V. Privitera, and G. Impellizzeri (2017). Mater. Sci. Semicond. Process. 69, 44.
17. M. I. Mohammed, R. M. Khafagy, M. S. Hussien, G. B. Sakr, M. A. Ibrahim, I. S. Yahia, and H. Y. Zahran (2022). *J. Mater. Sci: Mater. Electron*. 33, 1977.
18. A. Di Mauro, C. Farrugia, S. Abela, P. Refalo, M. Grech, L. Falqui, V. Privitera, and G. Impellizzeri (2020). Mater. Sci. Semicond. Process. 118, 105214.
19. A. Gupta, N. Khosla, V. Govindasamy, A. Saini, K. Annapurna, and S. R. Dhakate (2020). Appl. Nanosci. 10, 4191.
20. V. Varkey and E. T. Jose (2022). Polym. Plast. Tech. Mat. 61, 196.
21. N. Preda, A. Evanghelidis, M. Enculescu, C. Florica, and I Enculescu (2015). Mater. Lett. 138, 238.
22. E. Matei, C. Busuioc, A. Evanghelidis, I. Zgura, M. Enculescu, M. Beregoi, and I. Enculescu (2018). Appl. Surf. Sci. 458, 555.
23. Y. Liu, J. Jia, Y. V. Li, J. Hao, and K. Pan (2018). *Nanotechnology*. 29, 435704.
24. P. Pascariu, C. Cojocaru, P. Samoila, N. Olaru, A. Bele, and A. Airinei (2021). Mater. Res. Bull. 141, 111376.
25. M. A. Abu-Dalo, S. A. Al-Rosan, and B. A. Albiss (2021). *Polymers*. 13, 3451.
26. D. Morselli, P. Valentini, G. Perotto, A. Scarpellini, P. P. Pompa, A. Athanassiou, and D. Fragouli (2017). Compos. Sci. Technol. 149, 11.
27. R. Zamiri, A. Zakaria, H. A. Ahangar, M. Darroudi, A. K. Zak, and G. P. Drummen (2012). J. Alloys Compd. 516, 41.
28. S. Talam, S. R. Karumuri, and N. Gunnam (2012). *Int. Sch. Res. Notices*. 2012, 1.
29. B. D. Cullity and S. R. Stock (2001). *Prentice Hall. Upper Saddle River, NJ.* 388.
30. S. Ramesh, K. H. Leen, K. Kumutha, and A. K. Arof (2007). Spectrochim. Acta A Mol. Biomol. Spectrosc. 66, 1237.
31. V. V. Soman and D. S. Kelkar (2009). *Macromol. Symp.* 277, 152.
32. G. Xiong, U. Pal, J. G. Serrano, K. B. Ucer, and R. T. Williams (2006). Phys. Status. Solidi C. 3, 3577.

33. Z. G. Wang, X. T. Zu, S. Zhu, X. Xiang, L. M. Fang, and L. M. Wang (2006). Phys. Lett. A. 350, 252.
34. I. Kazeminezhad and A. Sadollahkhani (2016). J. Mater. Sci: Mater. Electron. 27, 4206.